INTERNATIONAL JOURNAL FOR NUMERICAL METHODS IN FLUIDS
Int. J. Numer. Meth. Fluids **30**: 279–308 (1999)

AN OVERLAPPING CONTROL VOLUME METHOD FOR THE NAVIER–STOKES EQUATIONS ON NON-STAGGERED GRIDS

ATUL KUMAR VERMA AND V. ESWARAN*

Department of Mechanical Engineering, Indian Institute of Technology, Kanpur 208016, India

SUMMARY

An algorithm, based on the overlapping control volume (OCV) method, for the solution of the steady and unsteady two-dimensional incompressible Navier–Stokes equations in complex geometry is presented. The primitive variable formulation is solved on a non-staggered grid arrangement. The problem of pressure–velocity decoupling is circumvented by using momentum interpolation. The accuracy and effectiveness of the method is established by solving five steady state and one unsteady test problems. The numerical solutions obtained using the technique are in good agreement with the analytical and benchmark solutions available in the literature. On uniform grids, the method gives second-order accuracy for both diffusion- and convection-dominated flows. There is little loss of accuracy on grids that are moderately non-orthogonal. Copyright © 1999 John Wiley & Sons, Ltd.

KEY WORDS: Navier–Stokes equations; control volume method; non-staggered grids

1. INTRODUCTION

The computation of viscous incompressible fluid flow in complex geometries is of interest to many branches of engineering. The use of boundary fitted grids allows selective refinement near the boundary walls, etc., and reduces storage, computational time, and improves accuracy. However, the implementation of finite difference schemes on body fitted co-ordinates requires mapping the complex domains onto a regular rectangular grid on which transformed equations are solved. The transformed equations are quite unwielding if the body fitted grid is not orthogonal. Therefore, other methods have been evolved that solve the governing equations in the physical domain itself, where the governing equations are much simpler than their counterparts in the transformed system.

In the primitive variable formulation, it has been the tradition [1] to use staggered grids to circumvent the problem of pressure–velocity decoupling. This decoupling [2] was the major difficulty associated with the non-staggered grid arrangement that hindered its applications to the solution of fluid flow problems. The successful application of non-staggered grids was reported by Hsu [3] and Rhie [4]. Rhie and Chows used *momentum interpolation* to overcome the problem of checkerboard pressure distribution. Peric [6], in addition, solved the governing partial differential equations on the physical domain in complex geometries.

* Correspondence to: Department of Mechanical Engineering, Indian Institute of Technology, Kanpur 208016, India.

CCC 0271–2091/99/110279–30$17.50

Received July 1997
Revised April 1998

The control volume based finite element methods [7–10] for arbitrary geometries combine the advantages of finite volume and finite element methods. Mukhopadhyay *et al.* [11] and Hwang [12] have developed noteworthy algorithms for flows in complex geometries without the use of global transformation of the physical domain and of the governing equations.

Recently, Verma and Eswaran [13] have introduced an overlapping control volume (OCV) technique for solving the steady convection–diffusion equation in arbitrary two-dimensional domains on non-orthogonal grids. The scheme was shown to have second-order accuracy in space and to be computationally efficient. Flux limiting has also been applied to the OCV formulation by Verma and Eswaran [14], who extended the previous work [13] to the explicitly time integrated transient case. The OCV scheme was also used to solve problems of multi-dimensional solute transport by implicit time stepping [15].

In this work, an OCV algorithm for computing steady and unsteady solutions to the two-dimensional incompressible Navier–Stokes equations on non-staggered grids is presented. The use of isoparametric interpolation is used to compute the diffusion terms and to introduce higher-order upwinding. However, the use of OCVs avoids the need for assembly, common in finite element algorithms and the method, in spirit, is a finite volume one. Since the problem is solved in the physical domain, the governing equations are much simpler than in the generalized co-ordinate system. An equal-order interpolation is used for the velocity components and pressure without encountering the problem that arises with interpolation in finite element formulations. The Cartesian components of velocities are used in the calculations, and thus the difficulties associated with the use of contravariant or covariant velocity components are avoided, without apparent loss in accuracy. This algorithm can be used to solve problems on non-orthogonal structured grids.

2. FORMULATION

The solution domain is discretized into a structured non-orthogonal grid as shown in Figure 1. A typical control volume is shown by the shaded area in the figure and also in Figure 1. These control volumes are referred to by the index of the central node, e.g. the control volume for (i, j) is shown in Figure 1(a). A non-staggered arrangement is used for the dependent variables, i.e. the pressure and each of the velocity components are defined at the same grid points.

2.1. Governing equations

The two-dimensional Navier–Stokes equations for laminar incompressible flow for an arbitrary control volume bounded by a closed line l can be expressed in the following integral form:

$$\oint_{cs} (\rho u_q)\, \mathrm{d}l_q = 0, \tag{1}$$

$$\frac{\partial}{\partial t}\iint (\rho u_q)\, \mathrm{d}A + \oint_{cs} (\rho u_q u_p)\, \mathrm{d}l_q - \oint \mu\left(\frac{\partial u_p}{\partial x_q} + \frac{\partial u_q}{\partial x_p}\right) \mathrm{d}l_q + \oint p\, \mathrm{d}l_q - \iint S_{u_p}\, \mathrm{d}a = 0, \tag{2}$$

where the Einstein summation convention is used and $p = 1, 2$, corresponds to the u_1, u_2 momentum equations for the x_1-, x_2-directions respectively. The components of the outward *normal* vectorial line element are $\mathrm{d}l_q$ and counterclockwise contour integration is assumed. Here, ρ represents the density of the fluid and S_{u_p} is the source term.

2.2. Discretization procedure

The discretization procedure for the continuity and momentum equations are described below.

2.2.1. Continuity equation. Equation (1) is discretized in the following way.

$$\oint_{cs} (\rho u_q)\, \mathrm{d}l_q \approx \sum_{k=1,2,3,4} (\rho u_1\, \mathrm{d}l_1 + \rho u_2\, \mathrm{d}l_2)^{(k)} = \sum_k (\rho u_1 \Delta x_2 - \rho u_2 \Delta x_1)^{(k)}, \tag{3}$$

where the superscript (k) refers to the edges of the control volume [shown circled in Figure 1(b)], $\Delta \mathbf{l}^{(k)} = (\Delta x_2 \mathbf{i} - \Delta x_1 \mathbf{j})^{(k)}$ is the normal surface vector of the kth cell edge, with $\Delta x_1^{(k)}$ and $\Delta x_2^{(k)}$ being the change in co-ordinates along edge k in the counterclockwise direction, and $u_1^{(k)}$ and $u_2^{(k)}$ are the velocity components defined at the midpoint of edge k.

In discretized form, the continuity equation can be expressed as

$$\sum_k F^{(k)} = F^{(1)} + F^{(2)} + F^{(3)} + F^{(4)} = 0, \tag{4}$$

where the $F^{(k)}$ is the outward mass flux through face (k):

$$F^{(k)} = \rho u_1^{(k)} \Delta x_2^{(k)} - \rho u_2^{(k)} \Delta x_1^{(k)}. \tag{5}$$

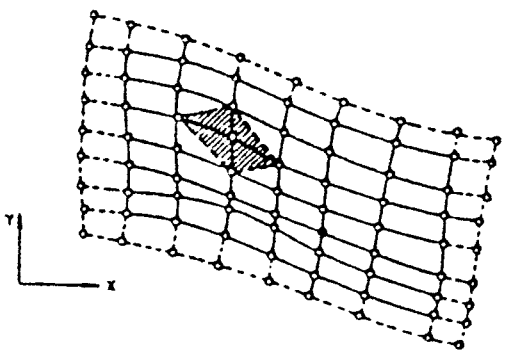

Figure 1(a)

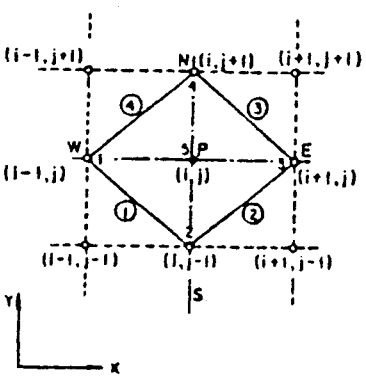

Figure 1(b)

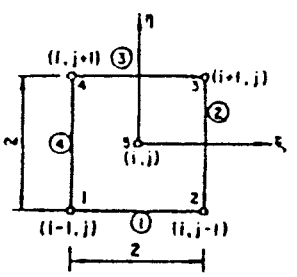

Figure 1(c)

Figure 1. Schematic diagram.

2.2.2. Rate of change term. The lumped mass approach is used for the transient term. The value of the velocity component u_p at the central node P of the control volume (CV) represents an average over the CV as a whole. Thus,

$$\frac{\partial}{\partial t}\iint \rho u_p \, \mathrm{d}A \approx \frac{(\rho u_p A_s)^{n+1} - (\rho u_p A_s)^n}{\Delta t} = \rho A_s \frac{(u_p)^{n+1} - (u_p)^n}{\Delta t}, \tag{6}$$

where A_s is the area of the cell.

2.2.3. Convection terms. The surface integral over the convection terms for u_p momentum equation is approximated using the midpoint rule; you get

$$\oint_{cs} (\rho u_q u_p) \, \mathrm{d}l_q \approx \sum_k (\rho u_p u_1 \Delta x_2 - \rho u_p u_2 \Delta x_1)^{(k)} = \sum_k u_p^{(k)} F^{(k)} \equiv \sum_k F_{pc}^{(k)}, \tag{7}$$

where $u_p^{(k)}$ is the value of u_p at the center of edge (k), and $F_{pc}^{(k)}$ is the outward *convected flux* of components u_p through edge k. To incorporate upwinding, $u_p^{(k)}$ in (7) is approximated at the midpoint of control surface k by interpolation within the *upwind* control volume at that surface. This scheme for convective modeling is conservative.

The method used for interpolation is based on finite element-type shape functions as explained in Verma and Eswaran [13]. The isoparametric formulation is used:

$$u_1 = \sum_{i=1}^{5} (u_1)_i N_i, \tag{8}$$

$$u_2 = \sum_{i=1}^{5} (u_2)_i N_i, \tag{9}$$

$$x_1 = \sum_{i=1}^{5} (x_1)_i N_i, \tag{10}$$

$$x_2 = \sum_{i=1}^{5} (x_2)_i N_i, \tag{11}$$

where $(x_1)_i$ and $(x_2)_i$ are the co-ordinates of the five grid points making the control volume. Equations (10) and (11) map the control volume in Figure 1(b) onto the transformed control volume in (ξ, η) co-ordinates shown in Figure 1(c) and N_i are shape functions defined in terms of these co-ordinates. For example,

$$N_1(\xi, \eta) = \frac{1}{4}(\xi\eta - \xi - \eta) + \frac{1}{8}(\xi^2 + \eta^2),$$

etc.

For the purposes of upwinding, $u_p^{(k)}$ is found by using Equations (8) and (9) to interpolate the value at the midpoint of the edge k in the transformed control volume.

To compute partial derivatives $\partial u_1/\partial x_1$, $\partial u_1/\partial x_2$, etc., there is a need to compute $\partial N_i/\partial x_1$, $\partial N_i/\partial x_2$ at the midpoint of the edges of the control volumes. These latter values are computed as part of the initialization procedure and stored for subsequent computations. The derivatives of any variable (ϕ) are determined from:

$$\frac{\partial \phi}{\partial x_1} = \sum_{i=1}^{5} \phi_i \frac{\partial N_i}{\partial x_1}, \tag{12}$$

$$\frac{\partial \phi}{\partial x_2} = \sum_{i=1}^{5} \phi_i \frac{\partial N_i}{\partial x_2}, \tag{13}$$

where ϕ_i are the values of ϕ at the ith node.

2.2.4. Diffusion flux. This term is also approximated using the midpoint rule. The discretized term from the u_1 momentum equation (2) is represented as

$$\oint \mu\left(\frac{\partial u_1}{\partial x_q}+\frac{\partial u_q}{\partial x_1}\right) \mathrm{d}l_q \approx \sum_k \left(2\mu \frac{\partial u_1}{\partial x_1}\Delta x_2 - \mu\left(\frac{\partial u_1}{\partial x_2}+\frac{\partial u_2}{\partial x_1}\right)\Delta x_1\right)^{(k)}$$
$$= \sum_k \left[2\mu \sum_k (u_1)_i \frac{\partial N_i}{\partial x_2}\Delta x_2 - \sum_i \mu\left((u_1)_i \frac{\partial N_i}{\partial x_2}+(u_2)_i \frac{\partial N_i}{\partial x_1}\right)\Delta x_1\right]^{(k)}$$
$$\equiv -\sum_k (F_{1d})^{(k)}, \tag{14}$$

where $F_{1d}^{(k)}$ is the diffusion flux of u_1 through edge k and is represented by the quantity in the square brackets. The diffusion flux of u_2, $F_{2d}^{(k)}$, is similarly represented in terms of (u_1, u_2) values at the nodes. The derivatives of the shape functions are evaluated at the midpoints, in (ξ, η) space, of the control surfaces. The summation is carried out over all the surfaces of the control volume. The diffusion modeling in OCV is second-order-accurate and has exactly the same error as the conventional five-point center difference discretization on a uniform grid.

2.2.5. Source term. It is assumed that the value at the central node represents the mean value over the whole control volume. Thus, the source term can be written as

$$\iint S_{u_p}\, \mathrm{d}A \approx (S_{u_p})_{ij} A_s.$$

Apart from the real source S_{u_p}, explicitly treated parts of the convection and diffusion fluxes may also be added to S_{u_p}, during iterations for the steady state or implicit solutions.

2.2.6. Pressure term. This term is treated explicitly in the predictor step (see below). For the u_1-momentum equation, the pressure term is

$$-\oint_{cs} p\, \mathrm{d}l_1 \approx -\sum_k p^{(k)} \Delta x_2^{(k)},$$

and for the u_2 equation, it is

$$-\oint_{cs} p\, \mathrm{d}l_2 \approx \sum_k p^{(k)} \Delta x_1^{(k)},$$

where $p^{(k)}$ is the pressure at the kth face center. In the correction step, gradient terms of the pressure corrections arise, which are treated analogously to the diffusion flux. This is explained in a later section.

3. TIME INTEGRATION SCHEME

Usually either semi-explicit or implicit Euler time integration schemes are used to discretize the time-dependent incompressible Navier–Stokes equations. In semi-explicit schemes, the momentum equations are discretized in an explicit manner, except for the pressure gradient terms, which are treated implicitly; the continuity equation is also enforced implicitly. As a consequence, the pressure–velocity coupling reduces effectively to a Poisson equation for the pressure corrections. Such schemes, because of their reliance on explicit time stepping, suffer

from time step restrictions. In implicit schemes, the equations are discretized fully implicitly, with the coupling being determined by the momentum equations. Some methods that fall within this latter group employ a sequential iteration (such as the SIMPLE method), in which the equations for each variable are repeatedly solved in succession.

Adopted here is a semi-explicit scheme in which the discretized equations

$$\rho(A_s)\frac{u_1^{n+1}-u_1^n}{\Delta t}+\sum_k (F_{1c}^n+F_{1d}^n)^{(k)} = -\sum_k [p^{n+1}]^{(k)}\Delta x_2^{(k)}+S_{u_1}^n A_s, \tag{15}$$

$$\rho(A_s)\frac{u_2^{n+1}-u_2^n}{\Delta t}+\sum_k (F_{2c}^n+F_{2d}^n)^{(k)} = \sum_k [p^{n+1}]^{(k)}\Delta x_1^{(k)}+S_{u_2}^n A_s, \tag{16}$$

have to be solved along with

$$\sum_k [F^{n+1}]^{(k)} = 0, \tag{17}$$

for each finite volume cell, where the superscript n refers to the (known) values at the current time step and $n+1$ to the (unknown) values at the next time level.

A two-step process is adopted. First, a predicted velocity u_1^* and u_2^* are found using the known n level values:

$$\rho(A_s)\frac{u_2^*-u_2^n}{\Delta t}+\sum_k (F_{1c}^n+F_{1d}^n)^{(k)} = -\sum_k [p^n]^{(k)}\Delta x_2^{(k)}+S_{u_1}^n A_s, \tag{18}$$

$$\rho(A_s)\frac{u_2^*-u_2^n}{\Delta t}+\sum_k (F_{2c}^n+F_{2d}^n)^{(k)} = \sum_k [p^n]^{(k)}\Delta x_1^{(k)}+S_{u_2}^n A_s. \tag{19}$$

Subtracting Equation (18) from (15), and (19) from (16), gives equations

$$\rho(A_s)\frac{u_1'}{\Delta t} = -\sum_k (p')^{(k)}\Delta x_2^{(x)}, \tag{20}$$

and

$$\rho(A_s)\frac{u_2'}{\Delta t} = \sum_k (p')^{(k)}\Delta x_1^{(x)}, \tag{21}$$

for the corrections

$$u_1' = u_1^{n+1}-u_1^*, \qquad u_2' = u_2^{n+1}-u_2^*, \qquad p' = u^{n+1}-p^*. \tag{22}$$

The corresponding flux corrections $(F')^{(k)}$ have to satisfy

$$\sum_k (F')^{(k)} = -\sum_k (F^*)^{(k)}, \tag{23}$$

where $(F^*)^{(k)}$ is the mass-flux corresponding to the predicted velocities, and $(F')^{(k)}$ is the perturbation due to the corrections in velocity and pressure. Equations (20), (21) and (23), have to be simultaneously solved by iterations. This cycle of iterations constitutes the corrector step in the time stepping. When the iterations converge, the corrected values are obtained from

$$u_1^{n+1} = u_1^* + u_1'$$
$$u_2^{n+1} = u_2^* + u_2',$$
$$p^{n+1} = p^* + p',$$

and the calculations proceed to the next time step.

3.1. Pressure–velocity corrections

Since a non-staggered, or collocated, arrangement is used in this formulation, the pressure–velocity decoupling or checkerboard pressure distribution may occur if the variables (velocities and pressure) at the cell edges are calculated by linear interpolation [2]. Rhie and Chow [5] used *momentum interpolation* to overcome this problem and opened a way toward the use of collocated grids for the solution of Navier–Stokes equations for incompressible flows in complex geometries. The authors, following similar lines, use a formulation in which the velocity at the cell faces are computed by allowing linear interpolation of the convective and diffusive terms but not of the pressure term. This is done in the following way:

If the discretized equation for predicted velocity in x_1-direction is written as

$$u_1^* = u_1^n + \frac{\Delta t}{\rho(A_s)}\left(-\sum_k (F_{1c} + F_{1d})^{(k)} + S_{u1} - \sum_k p^{(k)} \Delta x_2^{(k)} \right)^n, \tag{24}$$

where all terms on the right are nth time step values. The authors define a new variable U_1, which is computed using

$$U_1^* = u_1^n + \frac{\Delta t}{\rho(A_s)}\left(-\sum_k (F_{1c} + F_{1d})^{(k)} + S_{u1} \right)^n, \tag{25}$$

i.e. without the pressure term present in (24).

Now, to estimate the mass flux $(F^*)^{(1)}$ at the edge 1 (see Figure 1), straight forward linear interpolation would use

$$(F^*)^1_{\text{lin}} = \rho\overline{[((u_1^*)_{i-1,j}, (u_1^*)_{i-1,j})]}\,\Delta x_2^{(1)} - \rho\overline{[((u_2^*)_{i-1,j}, (u_2^*)_{i,j-1})]}\,\Delta x_1^{(1)}, \tag{26}$$

where the overbar indicates a linear interpolation. But the authors use

$$(F^*)^1 = \rho\overline{[((U_1^*)_{i-1,j}, (U_1^*)_{i-1,j})]}\,\Delta x_2^{(1)} - \rho\overline{[((U_2^*)_{i-1,j}, (U_2^*)_{i,j-1})]}\,\Delta x_1^{(1)} - \Delta t\left[\frac{\partial p^n}{\partial x_1}\right]^{(1)} \Delta x_2^{(1)} + \Delta t\left[\frac{\partial p^n}{\partial x_2}\right]^{(1)} \Delta x_1^{(1)}, \tag{27}$$

where the pressure derivatives are values at the midpoint of edge 1, and are estimated using Equations (12) and (13). This method thus avoids linear interpolation of pressure, implicit in (26); rather, it separates the pressure term using (25), and later incorporates it as a gradient term at the face, in Equation (27). This seemingly simple alteration effectively avoids pressure–velocity decoupling.

3.2. Time stepping algorithm

1. Initial conditions for velocity and pressure are prescribed; shape functions and derivative values are computed for each cell, etc.
2. Equations (24) and (25), and then counterparts for u_2, are used to compute the *predicted* cell center values of u_p^* and U_p^* for the next time step.
3. The *predicted* mass-flux through each cell edge k is computed using

$$(F^*)^{(k)} = \sum_j \rho U_j^{*(k)} l_j^{(k)} - \sum_j \Delta t\left(\frac{\partial p^n}{\partial x_j}\right)^{(k)} l_j^{(k)}, \tag{28}$$

where $U_j^{*(k)}$ is the linearly interpolated face value of U^*.

4. The flux correction at the edge k is computed by

$$(F')^{(k)} = -\Delta t \sum_j \left(\frac{\partial p'}{\partial x_j}\right)^{(k)} l_j^{(k)}, \tag{29}$$

using the isoparametric form (Equations (12)–(13)) to obtain the gradient of p' at the face (k). (Initially $p' = 0$, for each time step).

5. The mass-flux residual for each cell is computed by

$$\Re = -\sum_k (F^*)^{(k)} - \sum_k (F')^{(k)}. \tag{30}$$

6. The pressure correction for each node (i, j) is obtained from the relation

$$p' \leftarrow p' + \omega \frac{\Re}{a_{i,j}}, \tag{31}$$

where ω is a relaxation factor and $a_{i,j}$ is the diagonal coefficient obtained from the discretization of pressure in Equations (28)–(30).

7. If $\Re_{\text{rms}} > \epsilon$ goto Step 4.
8. Store the updated mass-flux through cell faces from

$$(F^*)^{(k)} \leftarrow (F^*)^{(k)} + (F')^{(k)} \tag{32}$$

(to be used to compute predicted velocities for the next time step).

9. Update pressure at the nodes (i, j), node $p^{n+1} \leftarrow p^n + p'$
10. Update velocity at nodes

$$u_j' = \frac{\Delta t}{\rho(A_s)} \sum_k (p')^{(k)} l_j^{(k)}, \tag{33}$$

$$u_j^{n+1} = u_j^* + u_j'. \tag{34}$$

11. $n \leftarrow n + 1$; goto Step 2 and repeat the process until steady state is reached.

The algorithm developed here is time-accurate, i.e. it can be used to solve unsteady flow problems. However, often such methods are used to solve steady state problems using the false-transient approach, i.e. starting from arbitrary fields and time marching to the steady state solutions.

In this algorithm, only pseudo pressure is solve for, not the true pressure. The pseudo pressure is obtained by using a rather simple homogeneous Neumann boundary condition instead of the complicated non-homogeneous, and *implicit* boundary condition needed for the true pressure. The true pressure often can be obtained from the pseudo pressure corrections, especially at high Reynolds number, although the boundary conditions used are not strictly *correct*. However, *even* if the pressure field is not accurately computed, e.g. at low Reynolds number, the correct divergence-free velocity field is nevertheless obtained (see, e.g. the velocity plots and pressure plots in Figures 20–25 below).

Also, the one-point iteration pressure correction scheme shown above may seem somewhat primitive, but it is robust and simple to implement. The pressure corrections can also be formulated as the solution of a Poisson equation, on which more efficient techniques may be used.

4. BOUNDARY CONDITIONS

The following types of boundary conditions, generally encountered in fluid flow problems, can be incorporated into this algorithm:

- no-slip boundary conditions:

$$u_p = 0;$$

- specified velocity boundary conditions:

$$u_p = u_0;$$

- free-slip boundary conditions:

$$u_n = 0, \qquad \frac{\partial u_t}{\partial n} = 0;$$

where n and t represents the normal and tangent components.

The boundary conditions for the pressure (p) and pseudo pressure correction (ψ') are

$$\begin{aligned} &\text{For pressure} && \frac{\partial p}{\partial n} = -\left[\frac{\mathrm{D}u_n}{\mathrm{D}t} - \frac{1}{Re}\nabla^2 u_n\right], \\ &\text{For the pseudo pressure correction} && \frac{\partial \psi'}{\partial n} = 0. \end{aligned} \tag{35}$$

It is convenient to use homogeneous boundary conditions, thus pseudo pressure is preferred here to get dynamically correct divergence-free velocity fields. However, to extract the true pressure field it is necessary to use correct boundary conditions for the pressure obtained from the Navier–Stokes equations as shown above.

At the exit boundary, for steady state flows the boundary conditions $\partial u_1/\partial x_1 = 0$, $\partial u_2/\partial x_1 = 0$, the so-called *fully developed flow* approximation, are used. At the inlet boundary, the inlet velocity is specified. Boundary conditions on solid walls are *no-slip* for velocity, and the pseudo pressure correction boundary conditions are as shown above.

5. RESULTS

The calculation procedure is applied here to five steady state and one unsteady flow problems. Four steady state test problems are solved on uniform grids, while one (the third) problem shows the efficacy of the method on non-orthogonal grids. The results in all cases are compared with either analytical solutions or with benchmark solutions reported in the literature. All solutions, including the steady state solutions, are obtained by time marching the unsteady governing equations:

$$\frac{\partial u}{\partial x} + \frac{\partial v}{\partial y} = 0, \tag{36}$$

$$\frac{\partial u}{\partial t} + u\frac{\partial u}{\partial x} + v\frac{\partial u}{\partial y} = -\frac{\partial \psi}{\partial x} + \frac{1}{Re}\nabla^2 u, \tag{37}$$

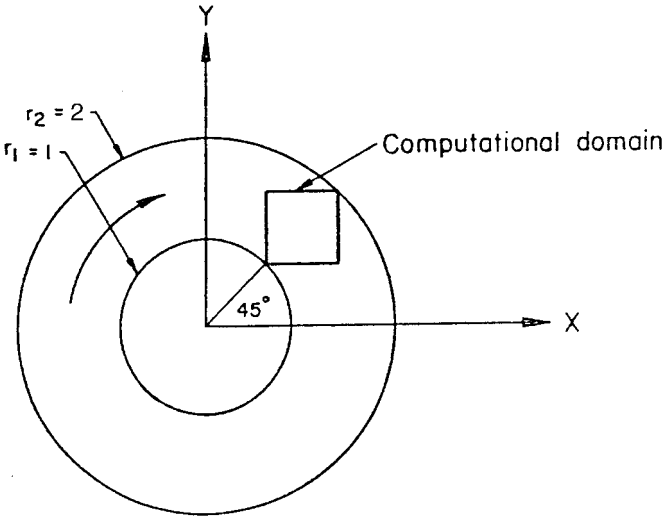

Figure 2. Schematic diagram of test problem 1.

$$\frac{\partial v}{\partial t} + u\frac{\partial v}{\partial x} + v\frac{\partial v}{\partial y} = -\frac{\partial \psi}{\partial y} + \frac{1}{Re}\nabla^2 v, \tag{38}$$

from the initial conditions

$$u = v = \psi = 0, \quad \text{at} \quad t = 0.$$

5.1. Flow between concentric rotating cylinders on uniform grids

The schematic of the problem is shown in Figure 2. The inner cylinder is at rest, while the outer cylinder rotates with angular velocity ω. The inner and outer radii of the rotating cylinders are r_1 and r_2 as shown in the figure. The exact solution of this problem is known and can be used to determine the accuracy of the computed solution. The aim is to solve this two-dimensional problem over the square region shown in Figure 2. The boundary conditions are of Dirichlet type for velocities and prescribed using the analytical solution. The homogeneous Neumann boundary condition has been used for the pseudo pressure. The analytical solution, which is independent of Reynolds number, is:

$$u = \frac{(2r - 2/r)y}{3r}, \tag{39}$$

$$v = \frac{(2r - 2/r)x}{3r}, \tag{40}$$

$$p = \frac{2(r^2 - 1/r^2) - 8\ln(r)}{9}, \tag{41}$$

where u, v and p are the two components of velocity, and pressure, non-dimensionalized by $2r$, ω and $\rho(2r\omega)^2$ respectively.

The computational domain is divided into $N \times N$ grid points. The results are obtained for four grids, $N = 11$, 21, 31 and 41. The Reynolds number ($Re = \rho(2r_1\omega)r_1/\mu$) is varied from 1 to 1000 and the radius ratio (r_2/r_1) is kept fixed at 2.

Table I. Percentage error in u at the center of domain

	Grid	$Re = 1$	$Re = 10$	$Re = 100$	$Re = 1000$
OCV	11×11	0.1171	0.1442	0.4169	0.6919
OCV	21×21	0.0289	0.0321	0.0431	0.0718
OCV	31×31	0.0128	0.0125	0.0199	0.0470
OCV	41×41	0.0071	0.0067	0.0109	0.0324
Baliga and Patankar [7]	21×21	0.020	0.034	0.264	0.287
Prakash and Patankar [8]	21×21	0.00404	0.0241	0.193	0.149

The variation of the absolute percentage error in u at the midpoint of the computational domain, and the average percentage of absolute error over the domain, with Reynolds number and grid size are tabulated in Tables I and II respectively. It can be seen that the method is second-order-accurate: doubling the grid (for fixed Reynolds number) reduces the error by at least a factor of 4. This is true for almost the entire range of Reynolds numbers from the diffusive ($Re = 1$) to the convective ($Re = 1000$) limits. The results obtained using OCV scheme are compared with the unequal-order method of Baliga and Patankar [7] (see Tables I and II) and the equal-order method of Prakash and Patankar [8] for 21×21 grid (see Tables I and II). It can be observed that the results obtained using the OCV approach compare well with those of these methods. If the average error (Table II), is expressed as $\epsilon \propto \Delta x^n$, where n is an exponent that roughly indicates the order of the scheme, one obtains $n = 2.01$, 2.16, 2.55, 2.13, for $Re = 1$, 10, 100, 1000 respectively, from the results displayed in Table II. It is clear that the method displays second-order accuracy on a uniform grid.

Figures 3–5 show a comparison of the analytical and computed solutions for the u-, v-velocity and pressure along the main diagonal of the computational domain for Reynolds number 1–1000. It can be observed that the computed solutions are in good agreement with the analytical solutions. Figures 6–11 show the computed solutions for u-, v-velocity and pressure along the main diagonal for three different grids 11×11, 21×21 and 41×41 for $Re = 10$ and 1000. The pressure computed is actually the pseudo pressure, i.e. it is obtained by using the homogeneous Neumann boundary conditions, but it seems to give good agreement with the analytical values except at the boundary points.

5.2. Flow in a driven square cavity

The problem considered here (Figure 12) is that of a two-dimensional square cavity of unit dimensions. The motion of an incompressible viscous fluid in the cavity is induced by the motion of the lid. Steady state two-dimensional laminar flow in a driven square cavity is a good benchmark problem because it offers a deceptively simple model on which numerical

Table II. Average percentage error in u over the domain

	Grid	$Re = 1$	$Re = 10$	$Re = 100$	$Re = 1000$
OCV	11×11	0.1222	0.1584	0.4611	0.5724
OCV	21×21	0.0296	0.0320	0.0508	0.0757
OCV	31×31	0.0131	0.0140	0.0224	0.0424
OCV	41×41	0.0075	0.0079	0.0134	0.0299
Baliga and Patankar [7]	21×21	0.034	0.060	0.407	0.594
Prakash and Patankar [8]	21×21	0.00846	0.0162	0.114	0.166

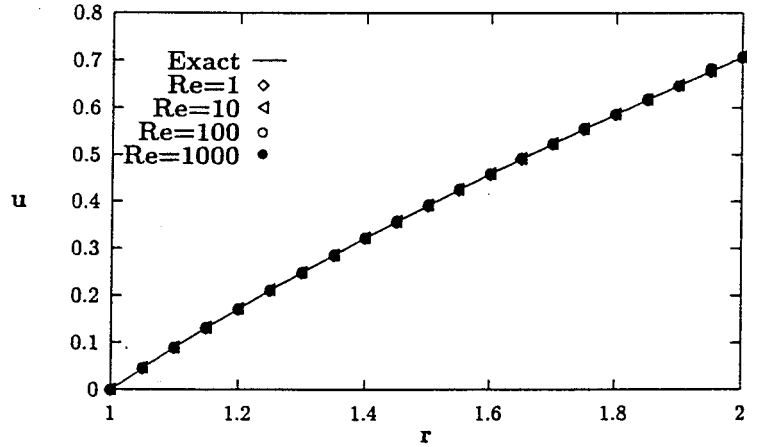

Figure 3. Variation of u-velocity along main diagonal (grid = 21 × 21).

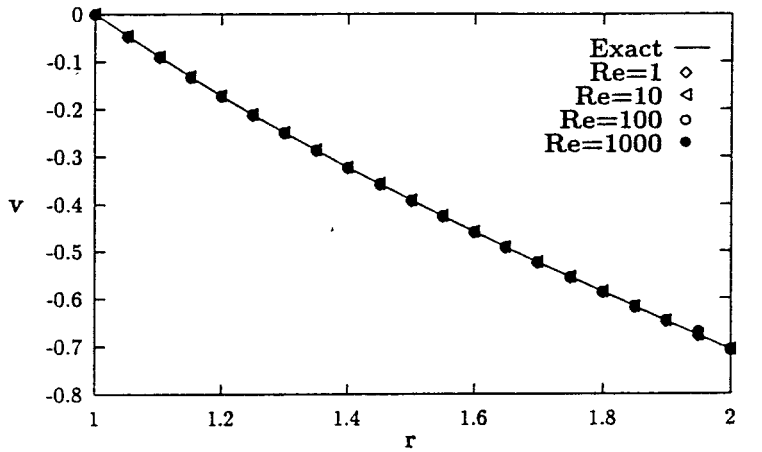

Figure 4. Variation of v-velocity along main diagonal (grid = 21 × 21).

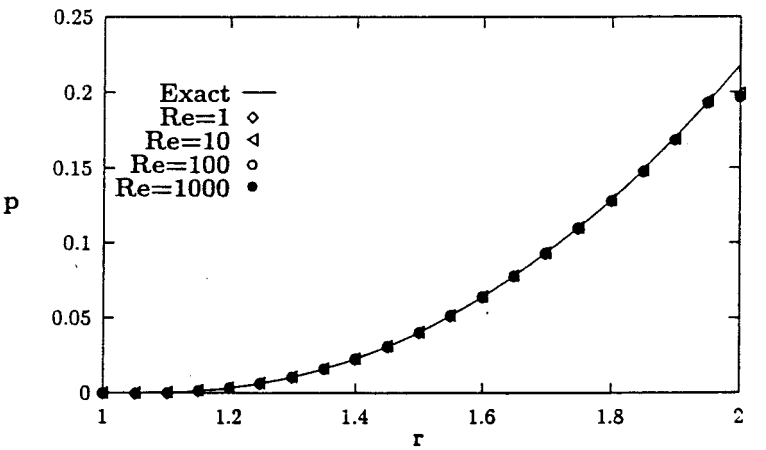

Figure 5. Variation of pressure along main diagonal (grid = 21 × 21).

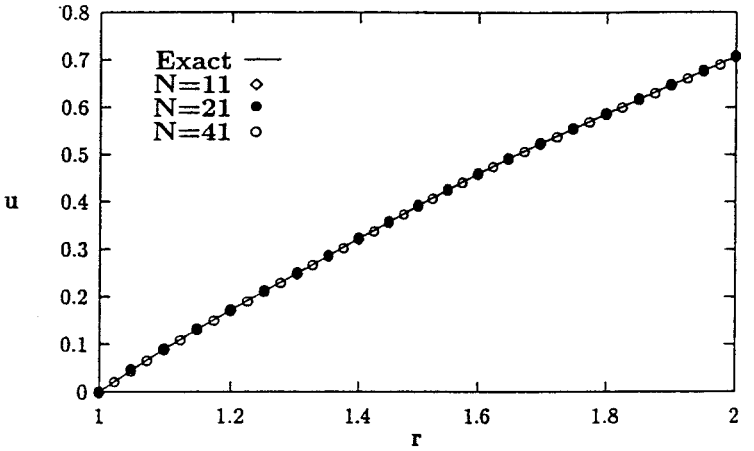

Figure 6. Variation of u-velocity along main diagonal for $Re = 10$.

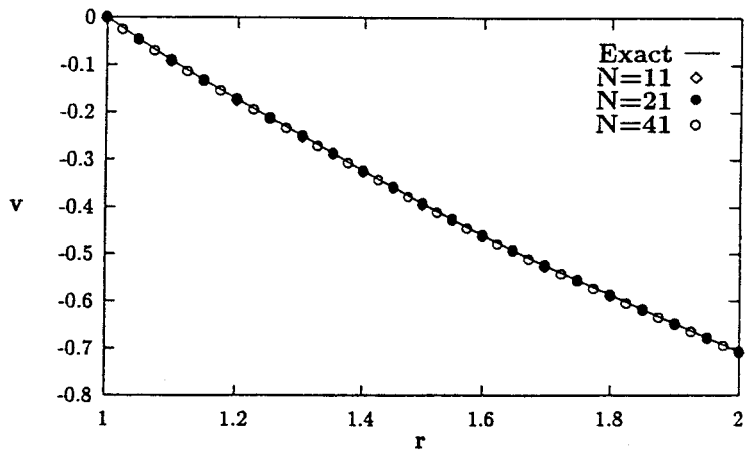

Figure 7. Variation of v-velocity along main diagonal for $Re = 10$.

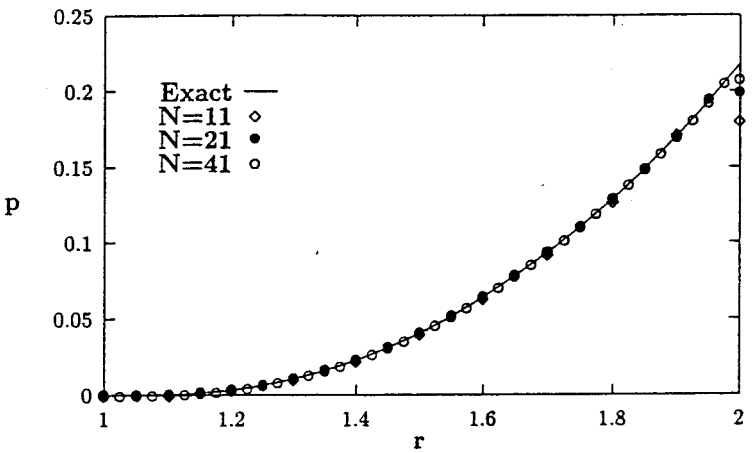

Figure 8. Variation of pressure along main diagonal for $Re = 10$.

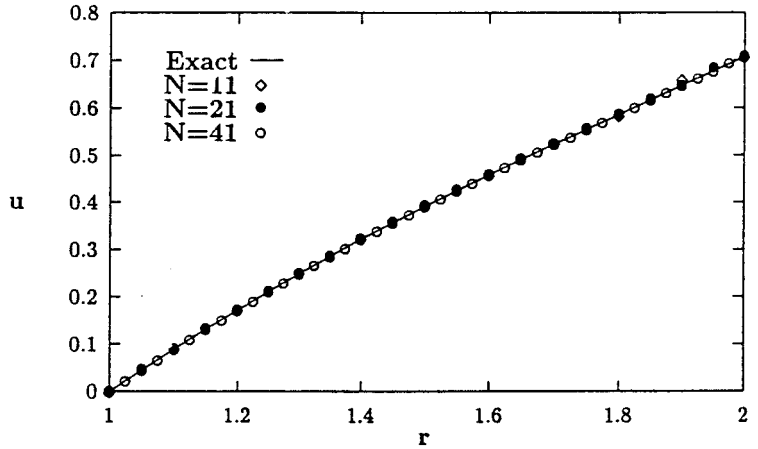

Figure 9. Variation of pressure along main diagonal for $Re = 1000$.

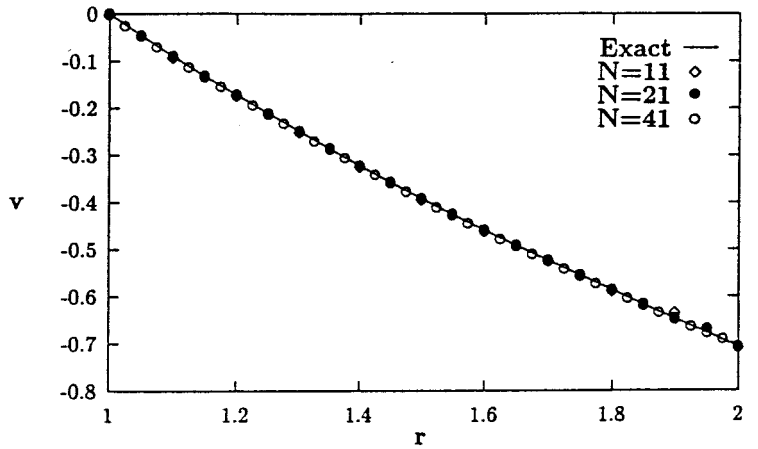

Figure 10. Variation of v-velocity along main diagonal for $Re = 1000$.

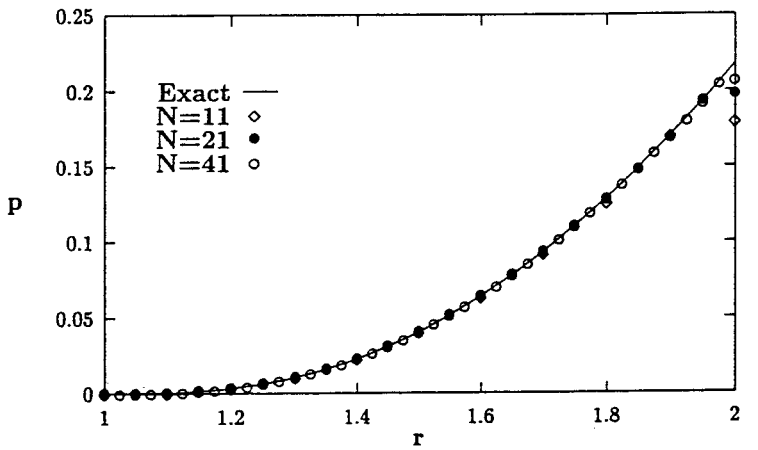

Figure 11. Variation of pressure along main diagonal for $Re = 1000$.

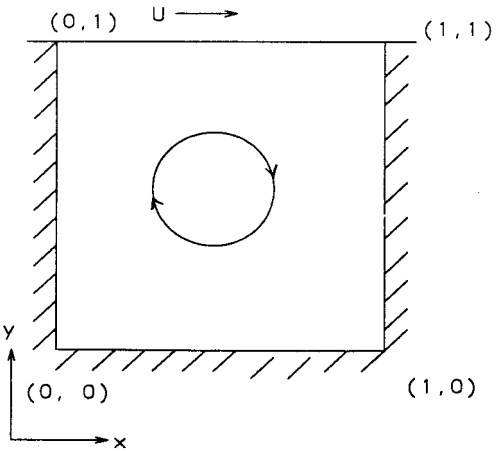

Figure 12. Schematic diagram of square cavity.

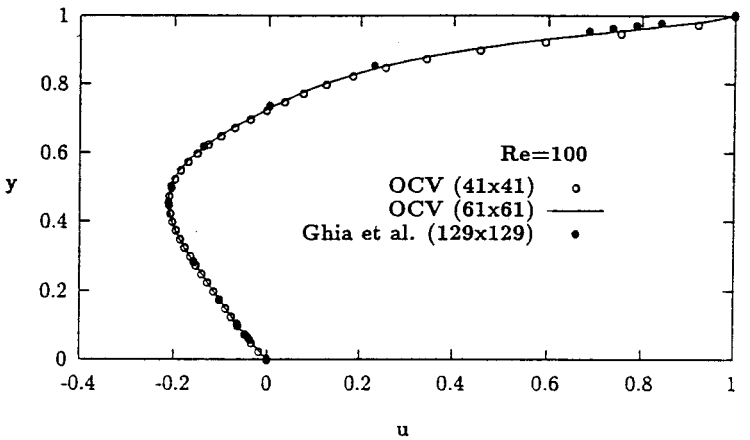

Figure 13. Velocity profiles on vertical centerline of a square cavity, $Re = 100$.

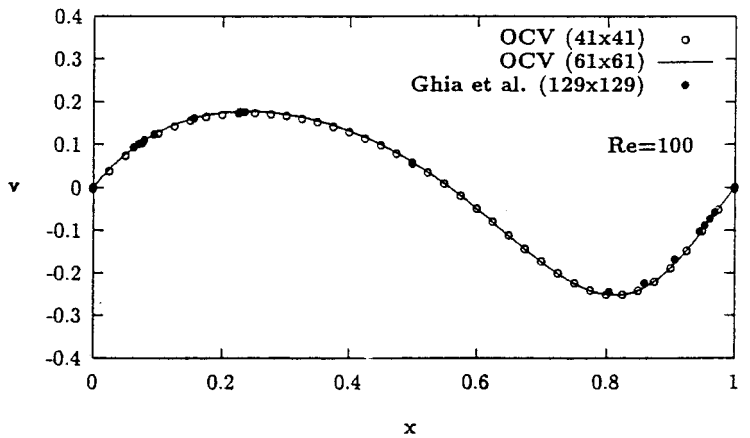

Figure 14. Velocity profiles on horizontal centerline of a square cavity, $Re = 100$.

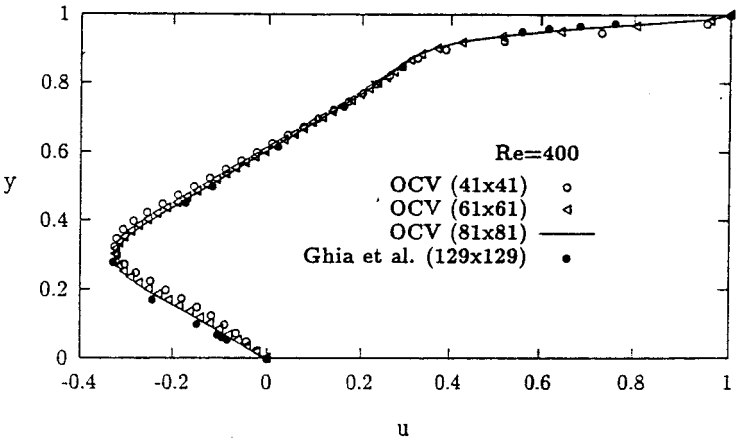

Figure 15. Velocity profiles on vertical centerline of a square cavity, $Re = 400$.

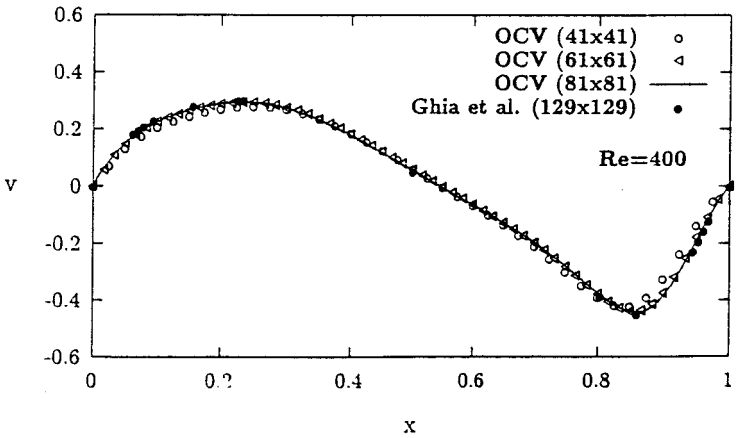

Figure 16. Velocity profiles on horizontal centerline of a square cavity, $Re = 400$.

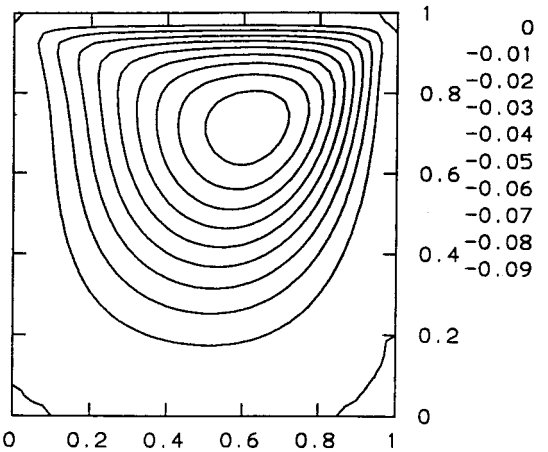

Figure 17. Streamlines in a lid-driven cavity for $Re = 100$ (41×41 grid).

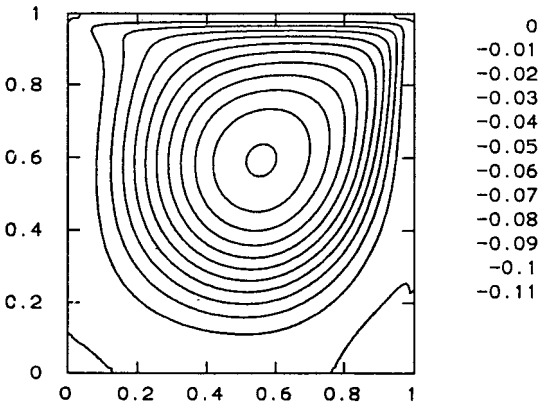

Figure 18. Streamlines in a lid-driven cavity for $Re = 400$ (81×81 grid).

techniques may be examined and very accurate numerical results are available for comparison (Ghia *et al.* [l6]).

The nature of the vortex formed in the cavity depends on the aspect ratio (cavity height to width ratio) as well as the Reynolds number ($Re \equiv Ud/v$), where U, d, v are the velocity of the top lid, width of the cavity (assumed to be unity) and the kinematic viscosity respectively.

The schematic of the problem is illustrated in Figure 12. The boundary conditions for the velocity components are given by

$$u = v = 0 \qquad \text{at} \quad x = 0, \quad x = 1,$$
$$u = v = 0 \qquad \text{at} \quad y = 0,$$
$$u = 1, \quad v = 0 \quad \text{at} \quad y = 1,$$

and $\partial\psi'/\partial n = 0$ on the solid boundaries. The velocities have been non-dimensionalized with U, and all lengths by the cavity width d.

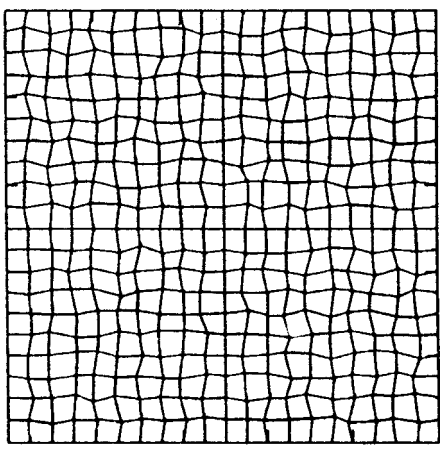

Figure 19. Distorted grid for test problem 3.

Table III. Average percentage error in u over the domain: OCV method (5% grid distortion)

Grid	$Re = 1$	$Re = 10$	$Re = 100$	$Re = 1000$
21×21	0.0296	0.0340	0.0827	0.1409
31×31	0.0132	0.0144	0.0290	0.0616
41×41	0.0075	0.0079	0.0140	0.0339

Table IV. Average percentage error in u over the domain: OCV method (10% grid distortion)

Grid	$Re = 1$	$Re = 10$	$Re = 100$	$Re = 1000$
21×21	0.0296	0.0338	0.0782	0.1979
31×31	0.0135	0.0142	0.0313	0.1190
41×41	0.0077	0.0078	0.0209	0.0866

Table V. Average percentage error in u over the domain: OCV method (20% grid distortion)

Grid	$Re = 1$	$Re = 10$	$Re = 100$	$Re = 1000$
21×21	0.0291	0.0205	0.1130	0.3348
31×31	0.0163	0.0165	0.0570	0.2426
41×41	0.0091	0.0092	0.0455	0.1383

The computational domain is divided into $N \times N$ uniform grids. The results have been obtained on grids corresponding to $N = 41$, 61 and 81, for Reynolds numbers of 100 and 400. Figures 13 and 14 show plots of the profiles of horizontal velocity along the vertical centerline and vertical velocity along the horizontal centerline of the cavity for $Re = 100$. Figures 15 and 16 show the results for $Re = 400$. The plots also show the finite difference results of Ghia *et al.* [16] on a finer grid of 129×129. It can be seen that the results obtained by OCV are in

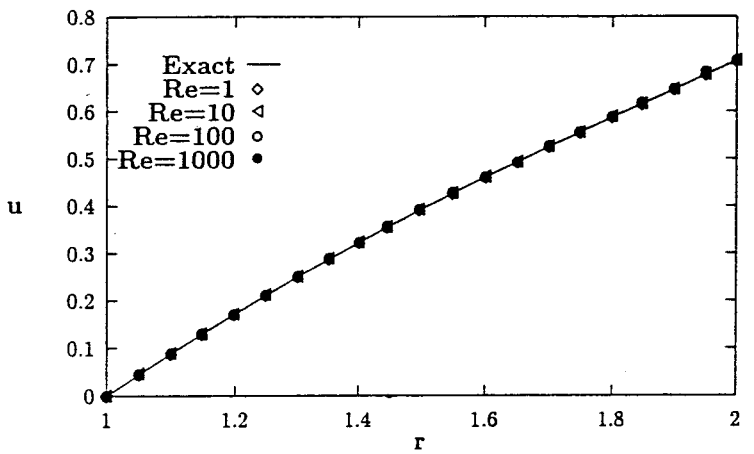

Figure 20. Variation of u-velocity along main diagonal on 10% distorted grid (21×21 grid).

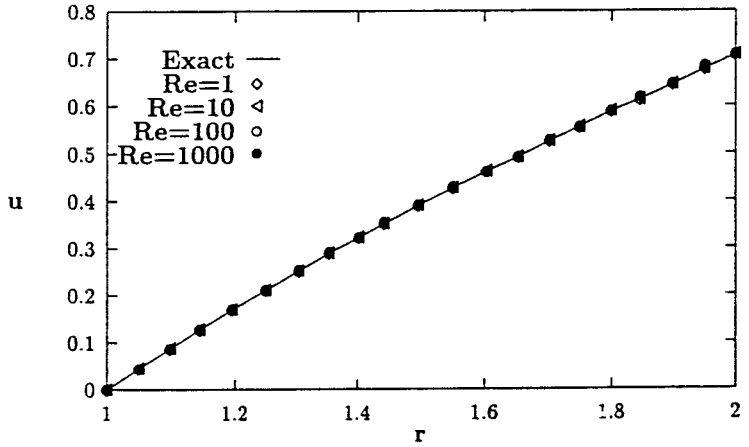

Figure 21. Variation of u-velocity along main diagonal on 20% distorted grid (21×21 grid).

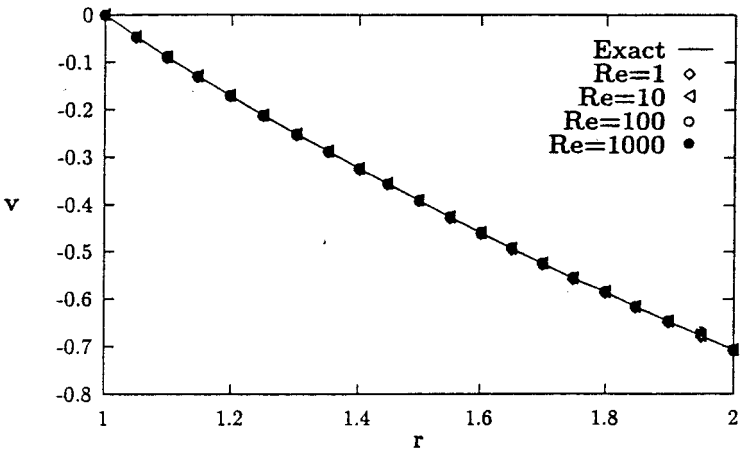

Figure 22. Variation of v-velocity along main diagonal on 10% distorted grid (21×21 grid).

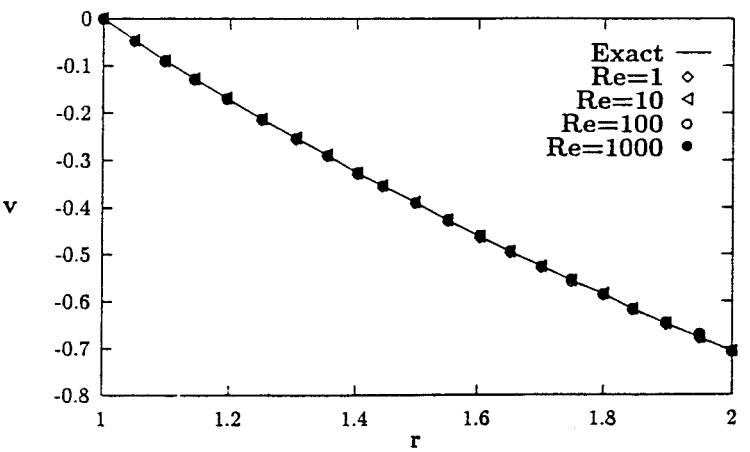

Figure 23. Variation of v-velocity along main diagonal on 20% distorted grid (21×21 grid).

close agreement with the reference solution. The streamlines for the flow of Reynolds number of 100 and 400 are shown in Figures 17 and 18. It can be observed that, for an aspect ratio of unity and relatively low Reynolds numbers, most of the strength of the vortex is

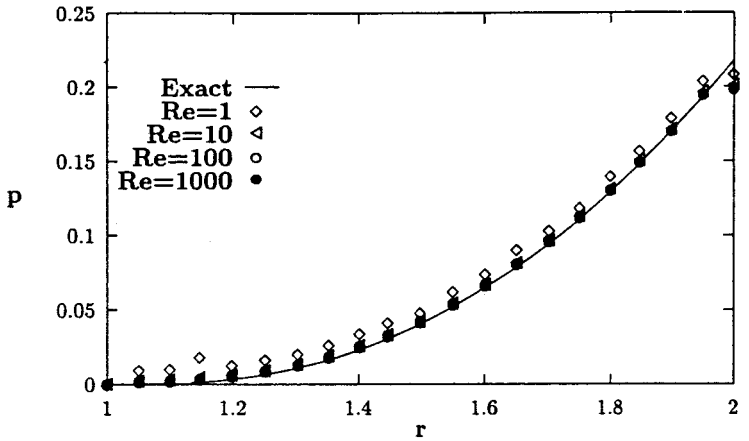

Figure 24. Variation of pressure along main diagonal on 10% distorted grid (21 × 21 grid).

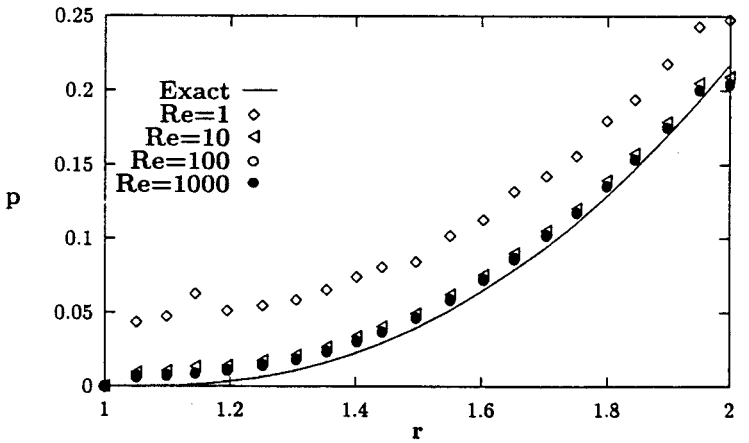

Figure 25. Variation of pressure along main diagonal on 20% distorted grid (21 × 21 grid).

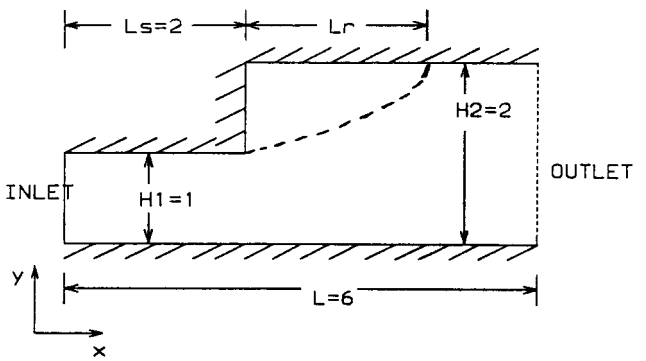

Figure 26. Schematic diagram of a channel with sudden expansion.

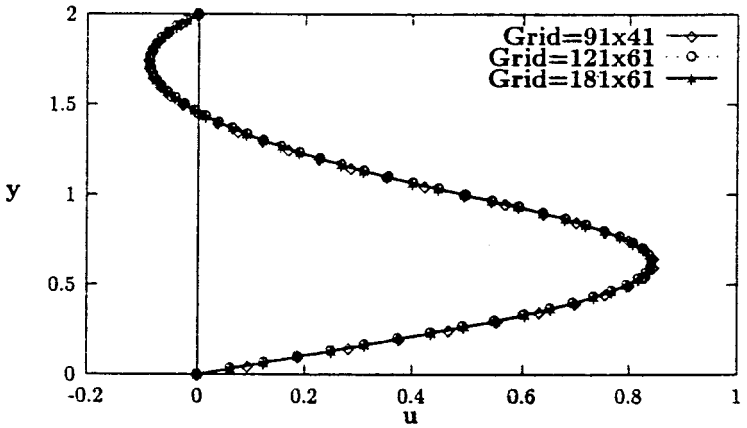

Figure 27. The u-velocity profile at $x = 3.0$.

concentrated in the upper portion of the cavity. As the Reynolds number increases, the vortex center moves downstream. With further increase in Reynolds number, the vortex center moves down and toward the center of the cavity. It can be clearly seen that the extent of the secondary circulation increases with the increase in the Reynolds number as expected.

5.3. Flow between concentric rotating cylinders on non-orthogonal grids

This problem is designed to test the applicability of the method to non-orthogonal grids. The details and exact solution of this problem is same as those of Test Problem 1. The only difference is the interior grid points are randomly perturbed from their original uniform grid positions to a maximum extent of 5, 10 and 20% of the average grid distance in both the directions. Figure 19 shows the 20% distorted grid.

The results for the above three distorted grids are presented in the Tables III, IV and V for $N = 21$, 31 and 41. The u velocity profiles along main diagonal of the domain are shown in Figures 20 and 21 for the 10% and 20% distorted grids respectively. Figures 22 and 23 show

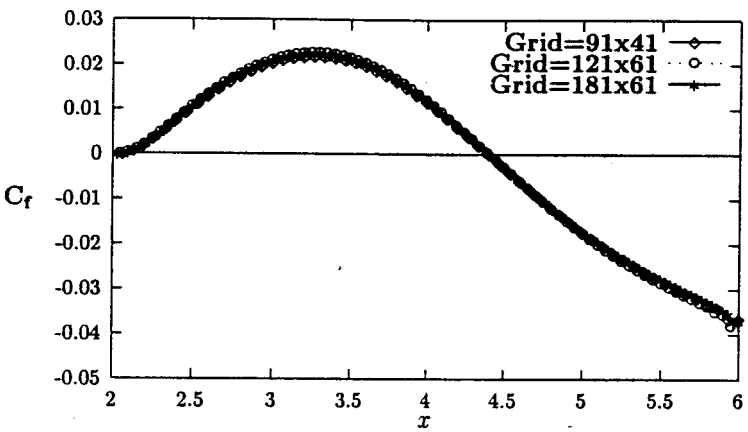

Figure 28. The variation of coefficient of friction along the top wall downstream from sudden expansion.

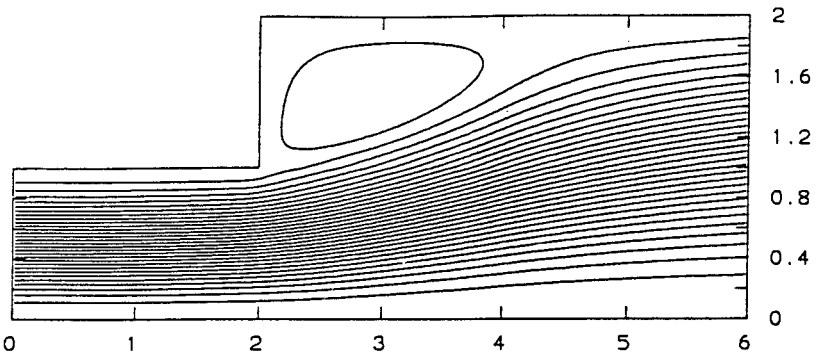

Figure 29. Streamlines plot for sudden expansion test case ($Re = 60$).

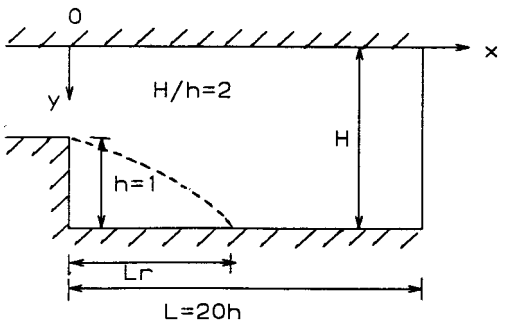

Figure 30. Schematic diagram of a channel with backward-facing step.

the corresponding v profile. There is little effect on the solution due to non-orthogonality of the grid. It is also observed that even on moderately non-orthogonal grids with 20% grid distortion, results obtained using OCV method is comparable with Baliga and Patankar [7] and Prakash and Patankar [8] (Tables I and II). The pseudo pressure plots are shown in Figures 24 and 25. It can be seen that the non-orthogonality causes the pseudo pressure solutions to differ from the analytical solutions. However, the magnitude of error decreases for higher Reynolds numbers, where the true pressure boundary condition is close to the homogeneous Neumann condition used in these computations.

Table VI. Reattachment length (L_r) vs. Re for backward-facing step

Method	Re	Grid	L	L_r
OCV	133	121×61	20.0	4.0
OCV	267	121×61	20.0	6.6
OCV	400	121×61	20.0	8.7
OCV	600	121×61	20.0	10.7
Reference [20]	133	256×64	12.0	4.0
Reference [20]	267	256×64	20.0	6.5
Reference [20]	400	256×64	27.0	8.5
Reference [20]	600	256×64	36.0	10.1
Reference [20]	400	512×128	27.0	8.7
Reference [20]	600	512×128	36.0	10.8

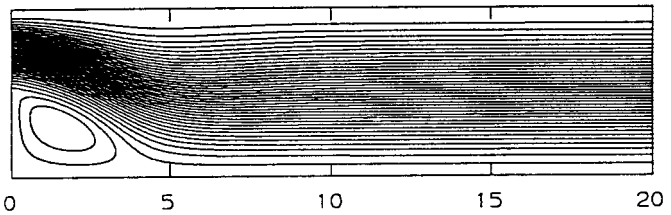

Figure 31. Streamlines plot for backward-facing step test case ($Re = 133$).

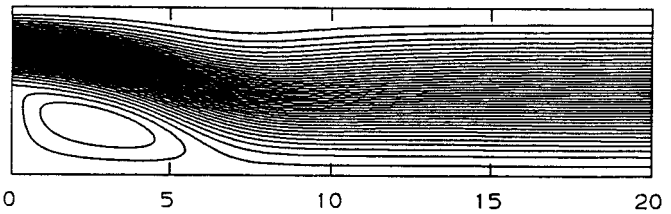

Figure 32. Streamlines plot for backward-facing step test case ($Re = 267$).

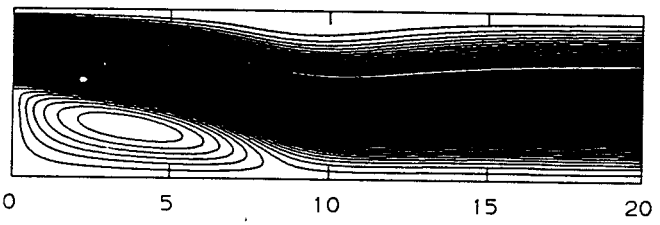

Figure 33. Streamlines plot for backward-facing step test case ($Re = 400$).

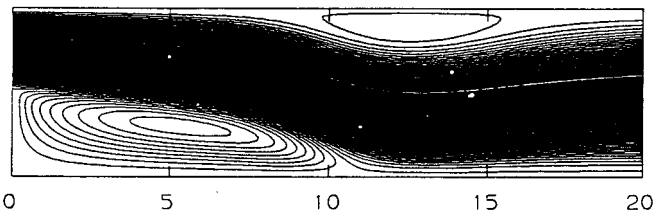

Figure 34. Streamlines plot for backward-facing step test case ($Re = 600$).

5.4. Flow through a channel with sudden expansion

The two-dimensional laminar flow over a sudden expansion/backward-facing step in a channel provides an excellent test case for the accuracy of numerical scheme because of the dependence of the reattachment length (L_r) on the Reynolds number. Excessive numerical diffusion, or smoothing in order to get numerical stability, will result in failure to predict the correct reattachment length. The schematic diagram for this problem is shown in Figure 26. The non-dimensional length of the channel (L) is 6 units and the non-dimensional height at the channel inlet (H_1) and outlet (H_2) are 1 and 2 units respectively, and the step is located at a downstream distance L_s of 2 units. The following boundary conditions have been used for the velocity components in the present computations:

$$u = 240y(1-y), \quad x = 0, \quad 0 \le y \le H_1; \quad v = 0, \quad x = 0, \quad 0 \le y \le H_1;$$
$$u = v = 0, \quad y = 0, \quad 0 \le x \le L; \quad u = v = 0, \quad y = H_1, \quad 0 \le x \le L_s;$$
$$u = v = 0, \quad x = L_s, \quad H_1 \le y \le H_2; \quad u = v = 0, \quad y = H_2, \quad L_s \le x \le L;$$

$$\frac{\partial u}{\partial x} = \frac{\partial u}{\partial y} = 0, \quad x = L, \quad 0 \le y \le H_2.$$

The computational domain, the 2×6 box enclosing the flow, is divided into a uniform grid. Three grids corresponding to 91×41, 121×61 and 181×61 grid points are used. The Reynolds number (based on the maximum velocity at inlet, $u_{max} = 60.0$) used for the computations is 60. The u-velocity profile at $x = 3$ units from the inlet section and coefficient of friction ($C_f = \tau_{wall}/[(1/2)\rho u_{max}^2]$) along the top wall in the sudden expansion zone are presented in Figures 27 and 28 respectively. These results are in close agreement with the results reported by Reddy *et al.* [17] for the same problem with a finite element method. The reattachment length, L_r, (where $C_f = 0$) obtained with the 91×41 and 181×61 grids are found to be 2.4060 and 2.4135 respectively, whereas Reddy *et al.* [17] obtained a value of 2.42093 by using a FRONTAL solver. The streamline plot is presented in Figure 29.

5.5. Flow through a channel with backward-facing step

This problem is essentially the same as the previous one, except that the details are changed so as to compare with the results of other researchers. The geometry and boundary conditions are shown in Figure 30. The step height is half the channel height and the step is located at $L_s = 0$, from the inlet. The Reynolds number is defined by $Re = u_{avg}H/v$. At the inflow boundary, located at the step, a parabolic profile $u(y) = 6y(1-y)$ is prescribed. This produces a maximum inflow velocity of $u_{max} = 1.5$ and average inflow velocity $u_{avg} = 1.0$. The experimental results for this particular flow configuration have been given by Armaly *et al.* [18] and numerical results can be found in the works of Kim and Moin [19], Thompson and Ferziger [20] and Gartling [21].

The steady state solutions for this problem have been obtained for Reynolds number values of 133, 267, 400 and 600. The number of grid points used in the computations, length of the channel and the calculated reattachment length (normalized by the step height) have been presented in Table VI. It can be seen that the predicted reattachment lengths (corresponding

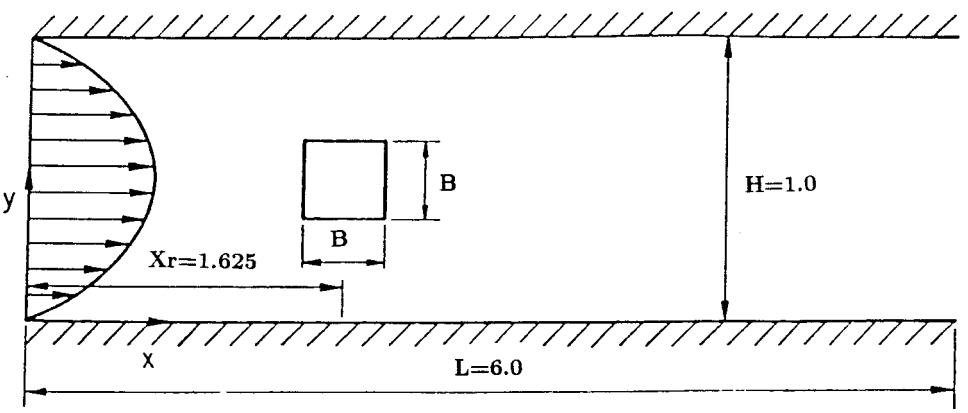

Figure 35. Schematic diagram of test problem 6.

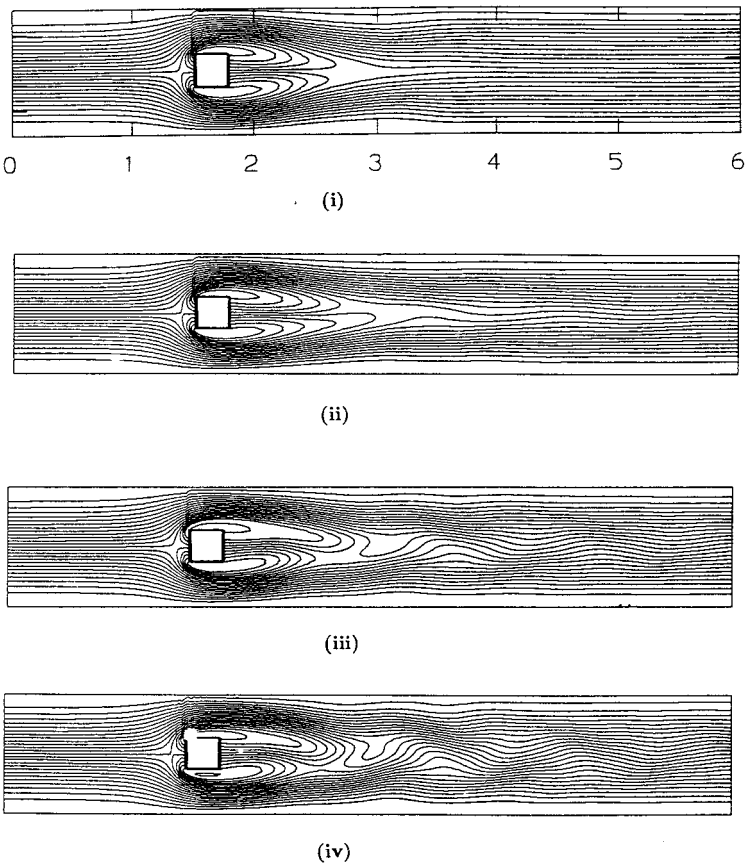

Figure 36. Streamline plots of the flow field for (i) $Re = 60$, (ii) $Re = 65$, (iii) $Re = 70$, (iv) $Re = 75$.

to $C_f = 0$) are very close to the values reported by Thompson and Ferziger [20] using 256×64 and 512×128 grid points as shown in Table IV.

The streamlines plots for various Reynolds numbers are shown in Figures 31–34. The size of the recirculation bubbles increases, as shown in the streamlines plots, with the Reynolds number. For larger Reynolds numbers, a secondary recirculation bubble is also observed on the top wall (see Figure 34). This is typical of the observations of the other researchers. The results obtained demonstrate that the OCV method is effective for recirculating incompressible fluid flow predictions.

5.6. Confined flow around square cylinder

Considered now is the unsteady flow around a square cylinder placed in a channel. This problem has been considered by a number of researchers [22–28]. The definition sketch for the problem is given in Figure 35. The relevant independent parameters are the blockage ratio (B/H) and the Reynolds numbers, here based on the average velocity ($Re = U_{avg}B/v$). At low Reynolds number, this problem can have steady state solutions. However, beyond a critical Reynolds number only unsteady solutions are possible, which involve alternate shedding of vortices from upper and lower downstream corners of the obstacle. The dependent variable of interest is the non-dimensional vortex shedding frequency, the Strouhal number $St \equiv fB/U_{avg}$,

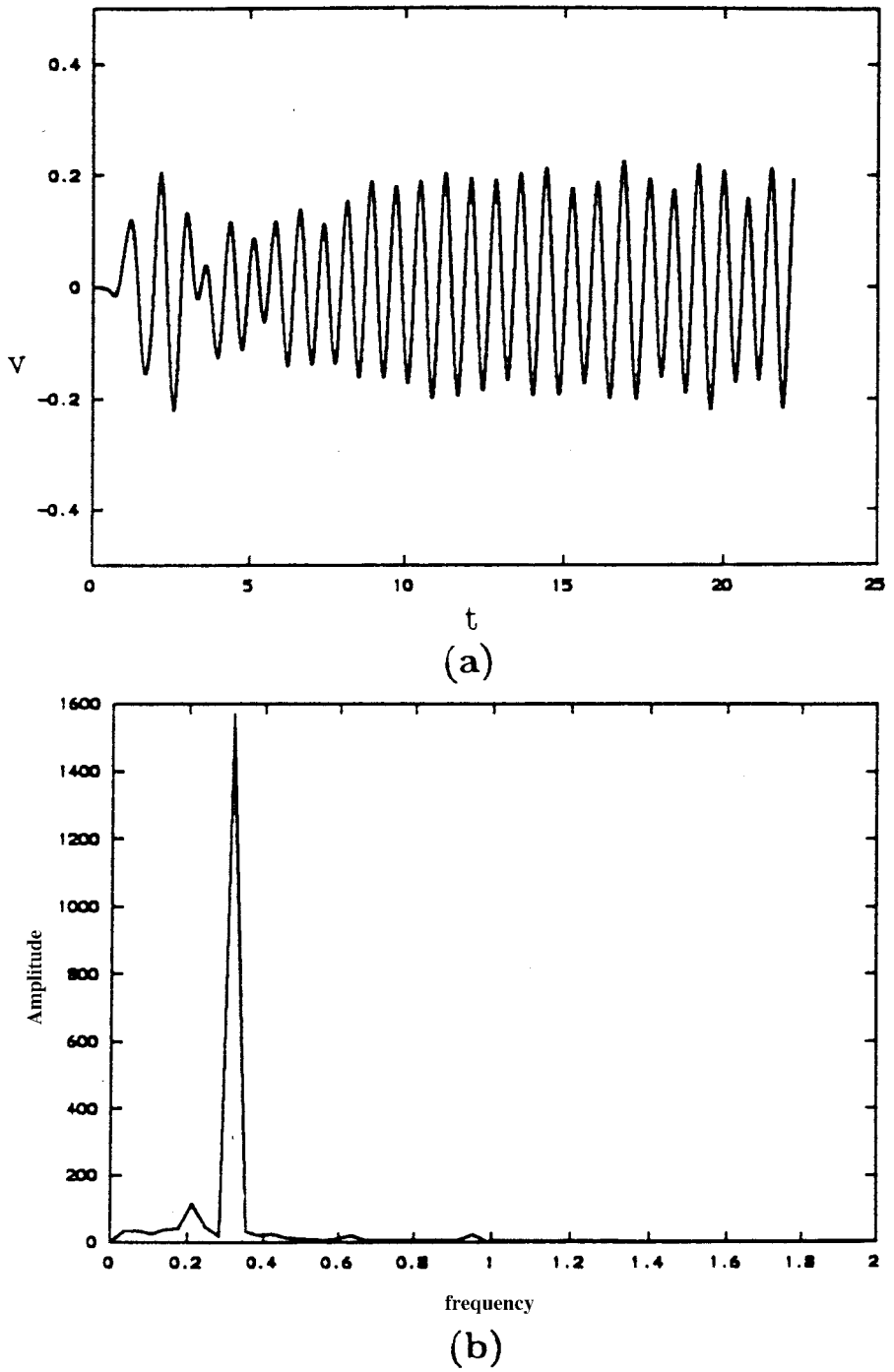

Figure 37. (a) Time variation of v-component of velocity on the centerline at a point $2B$ units behind the obstacle and (b) its spectra for Reynolds number of 375 and blockage ratio = 0.25.

where f is the frequency of the vertex shedding, and its dependence on the blockage ratio and Reynolds number. Also of interest are the critical Reynolds number, and their dependence on the blockage ratio and the time variation of the lift and drag coefficients, C_L and C_D, which relate to the vortex shedding in the wake of the cylinder.

The attempt here, however, is not to repeat the extensive study done on this problem by others (e.g. Davis and Moore [22]). This paper's purpose is to validate the OCV algorithm on this unsteady problem and computations for only a limited range of parameters are performed in order to establish that the results obtained are comparable with those reported in the

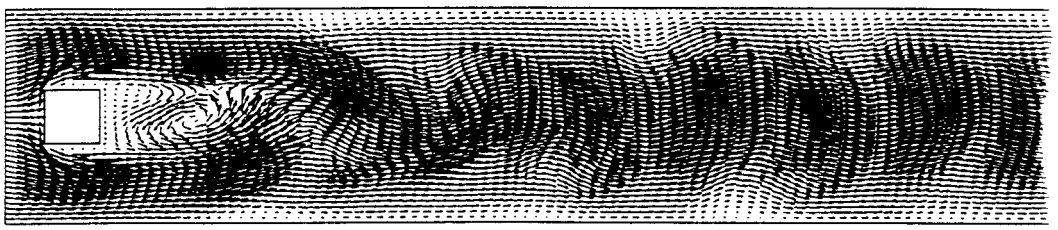

(a)

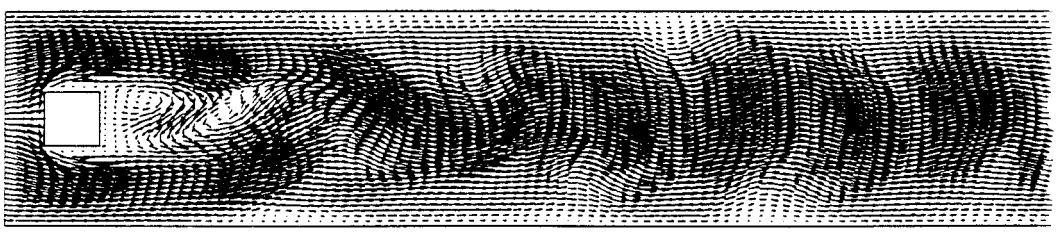

(b)

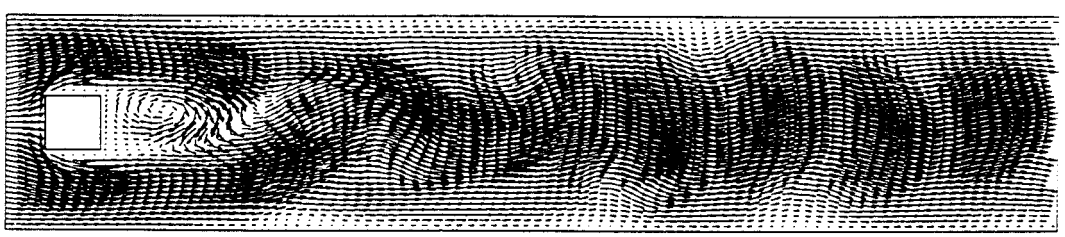

(c)

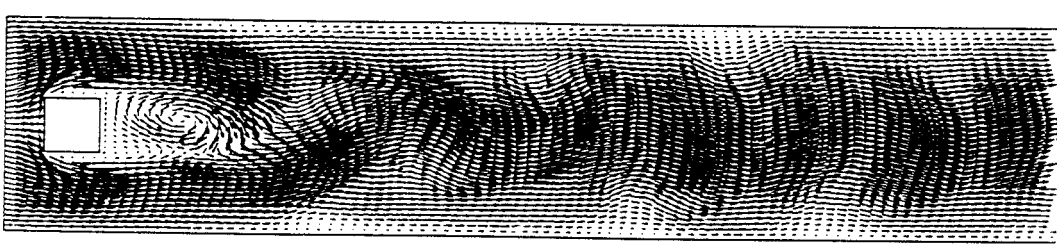

(d)

Figure 38. Velocity vector plot for test problem 6 ($Re = 150$ and $B/H = 0.25$).

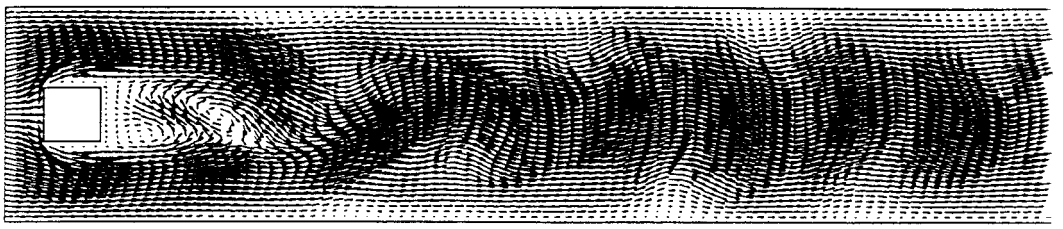

(e)

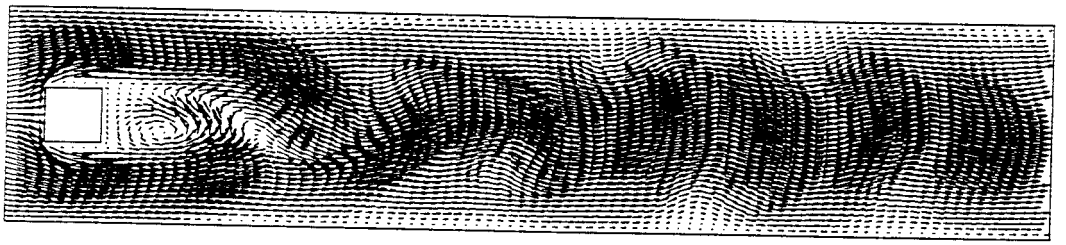

(f)

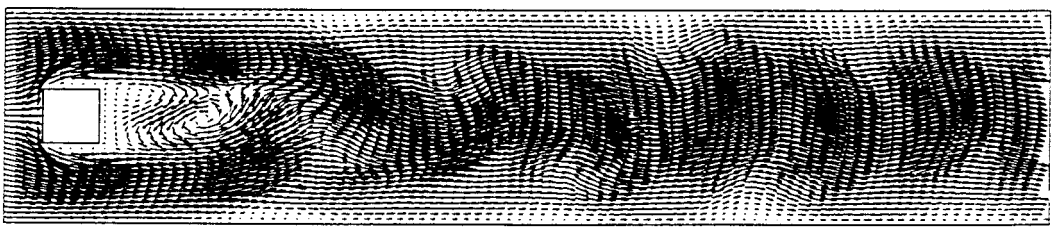

(g)

Figure 38 (*Continued*)

literature. So, the present computations are confined to cases with a blockage ratio of 0.25, Reynolds numbers of 50–375 on a 241×81 uniform grid.

For the purposes of computations, a parabolic profile is assumed at the inlet, no-slip conditions at the walls and at the obstacle, and the outlet boundary conditions imposed at the outlet ($L/B = 24.0$) are the convective boundary conditions as proposed by Orlanski [29]. The equations being solved are (36)–(38), in which pseudo pressure ψ is used. The boundary conditions for ψ are $\psi = 0$ at the exit and homogeneous Neumann on the solid walls, obstacle and the inlet. The use of pseudo pressure simplifies the boundary conditions, but at the cost of are not being able to compute C_L and C_D, which require knowledge of the true pressure.

Figure 36 shows the streamfunction plots of the flow field for Reynolds number of 60, 65, 70 and 75 respectively, all for a blockage ratio of 0.25. It may be observed that the flow is steady (and symmetrical) for Reynolds number of 60, while for $Re = 65$ and above, signs of unsteadiness and vortex shedding appear. Thus, in the authors calculations for the assumed blockage ratio, the critical Reynolds number is around 65. Davis *et al.* [22] numerically obtained a critical Reynolds number, based on a centerline velocity of about 100.0, which corresponds to $Re = 66.66$, as per the authors definition of Reynolds number. This seems to

validate the figure. Mukhopadhyay *et al.* [26] obtains a critical Reynolds number of 85 using the EXTRA–FLAG science. However, that scheme was somewhat more diffusive than the OCV scheme and numerical diffusion causes as overprediction of the critical Reynolds number.

Figure 37 shows the time variation of the v component of velocity on the centerline at a point $2B$ units behind the obstacle, for a typical case (Reynolds number of 475 and blockage ratio of 0.25) and its corresponding spectra is shown in Figure 37(b). It may be seen that the velocity variation is essentially periodic with a single dominant frequency. The Strouhal number computed from these results for Reynolds number of 150 is 0.2868. Davis *et al.* [22] obtained a Strouhal number of 0.2625 numerically and 0.302 experimentally for a Reynolds number of 166.6. (Their definition of Reynolds number and Strouhal number are based on centerline velocity U_0 and are here converted into the present one by assuming $U_0 = 1.5U_{\text{avg}}$). Mukhopadhyay *et al.* [26] obtains a somewhat lower Strouhal number of 0.2384 for the same case ($Re = 150$ and blockage ratio $= 0.25$). In the present calculations, Strouhal number values of 0.2723 and 0.3168 for Reynolds number of 75 and 375 respectively, are also obtained. Figure 38(a)–(g) shows a velocity plot spanning an entire cycle of vortex shedding for Reynolds number 150 and blockage ratio of 0.25. The figures show qualitatively much the same behavior as reported in the literature.

6. CONCLUSIONS

An algorithm for computing steady and unsteady solutions to the two-dimensional incompressible Navier–Stokes equations on non-staggered grids in primitive variable formulation has been presented. This algorithm works well on both orthogonal and non-orthogonal grids. The salient features of this study have been summarized below.

(1) The physical domain is discretized into overlapping control volumes. Since control volumes are formed by taking the grid points as the vertices of the cells, grid point information is directly used to compute geometrical parameters.

(2) Since the problem is solved in the physical domain, the governing partial differential equations are simpler than their counterpart in the generalized co-ordinate system.

(3) An isoparametric description of the variables and geometry have been used. However, the spirit of the method is that of finite volume rather than that of finite element methods, as no assembly is used.

(4) The Cartesian components of velocities are used in the calculations and there are no complications associated with the use of covariant or contravariant components of velocities.

(5) An equal-order interpolation is used for the velocity components and pressure. The problem of checkerboard pressure distribution is avoided by using *momentum interpolation*.

(6) The proposed method is validated by computing the laminar flow in six test cases. In all cases, computed results exhibit good agreement with reference solutions.

(7) The applicability of the method to non-orthogonal grids is also demonstrated. The accuracy of the solution is not very sensitive to the moderate grid non-orthogonality.

(8) The algorithm has also been shown to be effective in obtaining unsteady solutions for the non-trivial problem of predicting vortex shedding behind a square cylinder. The results obtained match well with those in literature.

REFERENCES

1. F.H. Harlow and J.E. Welch, 'Numerical calculation of time-dependent viscous incompressible flow of fluid with free surface', *Phys. Fluids*, **8**, 2182–2188 (1965).
2. S.V. Patankar, *Numerical Heat Transfer and Fluid Flow*, Hemisphere, New York, 1980.
3. C.F. Hsu, 'A curvilinear co-ordinate method for momentum heat and mass transfer in domains of irregular geometry', *Ph.D. Thesis*, University of Minnesota, 1981.
4. C.M. Rhie, 'A numerical study of flow past an isolated airfoil with separation', *Ph.D. Thesis*, University of Illonois, Urbana-Champaign, 1981.
5. C.M. Rhie and W.L. Chow, 'Numerical study of the turbulent flow past an airfoil with trailing edge separation', *AIAA J.*, **21**, 1525–1532 (1983).
6. M. Peric, 'A finite volume method for prediction of three dimensional fluid flow in complex ducts', *Ph.D. Thesis*, University of London, 1985.
7. B.R. Baliga and S.V. Patankar, 'A control volume finite element method for two-dimensional fluid flow and heat transfer', *Numer. Heat. Transf.*, **6**, 245–261 (1983).
8. C. Prakash and S.V. Patankar, 'A control volume-based finite element method for solving the Navier–Stokes equations using equal-order velocity–pressure interpolation', *Numer. Heat Transf.*, **8**, 259–280 (1985).
9. C. Prakash, 'An improved control volume finite element method for heat and mass transfer and for fluid flow using equal order velocity–pressure interpolation', *Numer. Heat. Transf.*, **9**, 253–276 (1986).
10. G.E. Schneider and M.J. Raw, 'Control volume finite element method for the heat transfer and fluid flow using collocated varaibles—1. Computational procedure', *Numer. Heat Transf.*, **11**, 363–390 (1987).
11. A. Mukhopadhyay, T. Sundararajan and G. Biswas, 'An explicit transient algorithm for predicting incompressible flows in arbitrary geometry', *Int. J. Numer. Methods Fluids*, **17**, 975–993 (1993).
12. Y.H. Hwang, 'Arbitrary domain velocity analyses for the incompressible Navier–Stokes equations', *J. Comput. Phys.*, **110**, 134–149 (1994).
13. Atul Kumar Verma and V. Eswaran, 'Overlapping control volume approach for convection–diffusion equation', *Int. J. Numer. Methods Fluids*, **23**, 865–882 (1996).
14. Atul Kurmar Verma and V. Eswaran, 'A bounded scheme for overlapping control volume approach', *Int. J. Numer. Methods Fluids*, **25**, 1137–1161 (1997).
15. Atul Kumar Verma, S. Bhallamudi Murty and V. Eswaran, 'Overlapping control volume approach for solute transport problems', communicated.
16. U Ghia, K.N. Ghia and C.T. Shin, 'High-resolutions for incompressible flow using the Navier–Stokes equations and a multigrid method', *J. Comput. Phys.*, **48**, 387–411 (1982).
17. M.P. Reddy, L.G. Reifschneider, J.N. Reddy and H.U. Akay, 'Accuracy and convergence of element-by-element iterative solvers for incompressible fluid flows using penalty finite element model', *Int. J. Numer. Methods. Fluids*, **17**, 1019–1033 (1993).
18. B.F. Armaly, F. Durst, J.C.F. Pereira and B. Schonung, 'Experimental and theoretical investigation of backward-facing step flow', *J. Fluid Mech.*, **172**, 473–496 (1983).
19. J. Kim and P. Moin, 'Application of a fractional step method to incompressible Navier–Stokes equations', *J. Comput. Phys.*, **59**, 308–323 (1985).
20. M.C. Thompson and J.H. Ferziger, 'An adoptive multigrid technique for the incompressible Navier–Stokes equations', *J. Comput. Phys.*, **82**, 94–121 (1989).
21. D.K. Gartling, 'A test problem for outflow boundary conditions—Flow over a backward facing step', *Int. J. Numer. Methods Fluids*, **11**, 953–967 (1990).
22. R.W. Davis, E.F. Moore and L.P. Purtell, 'A numerical–experimental study of confined flow around rectangular cylinders', *Phys. Fluids*, **27**, 46–59 (1984).
23. A. Okajima, 'Strouhal numbers of rectangular cylinders', *J. Fluid Mech.*, **123**, 379–398 (1982).
24. A. Okajima, 'Numerical simulation of flow around rectangular cylinders', *J. Wind Eng. Ind. Aerodynam.*, **33**, 171–180 (1990).
25. T. Tamura, 'Numerical study of aerodynamic behaviour of a square cylinder', *J. Wind Eng. Ind. Aerodynam.*, **33**, 161–170 (1990).
26. A. Mukhopadhyay, G. Biswas and T. Sundarajan, 'Numerical investigation of confined wakes behind a square cylinder in a channel', *Int. J. Numer. Methods Fluids*, **14**, 1473–1484 (1992).
27. K.M. Kelkar and S.V. Patankar, 'Numerical prediction of vortex shedding behind a square cylinder', *Int. J. Numer. Methods Fluids*, **14**, 327–341 (1992).
28. G. Li and J.A.C. Humphrey, 'Numerical modelling of confined flow past a cylinder of square cross-section at various orientations', *Int. J. Numer. Methods Fluids*, **20**, 1215–1236 (1995).
29. I. Orlanski, 'A simple boundary condition for unbounded hyperbolic flows', *J. Comput. Phys.*, **21**, 251–269 (1976).

